JGR Oceans

RESEARCH ARTICLE
10.1029/2023JC020175

Interactions Between Internal Solitary Waves and Sea Ice

Samuel G. Hartharn-Evans[1,2], Magda Carr[1], and Marek Stastna[3]

[1]School of Mathematics, Statistics and Physics, Newcastle University, Newcastle upon Tyne, UK, [2]Department of Geography and Environmental Sciences, Northumbria University, Newcastle upon Tyne, UK, [3]Department of Applied Mathematics, University of Waterloo, Waterloo, ON, Canada

Key Points:

- Internal Solitary Waves (ISWs) can interact with sea ice in the Arctic Ocean. This process is modeled using laboratory experiments
- The wave-induced motion of ice is slower when the ice length is large in comparison to the wave, a result explained by the wave form alone
- Vortices form at the ice edge. They are boundary layer features that depend on the motion of both the ice and ISW

Supporting Information:

Supporting Information may be found in the online version of this article.

Correspondence to:

S. G. Hartharn-Evans,
sam.hartharn-evans@northumbria.ac.uk

Citation:

Hartharn-Evans, S. G., Carr, M., & Stastna, M. (2024). Interactions between internal solitary waves and sea ice. *Journal of Geophysical Research: Oceans*, *129*, e2023JC020175. https://doi.org/10.1029/2023JC020175

Received 27 JUN 2023
Accepted 14 DEC 2023

Author Contributions:

Conceptualization: Samuel G. Hartharn-Evans, Magda Carr
Data curation: Samuel G. Hartharn-Evans
Formal analysis: Samuel G. Hartharn-Evans
Funding acquisition: Magda Carr
Investigation: Samuel G. Hartharn-Evans, Magda Carr
Methodology: Samuel G. Hartharn-Evans, Magda Carr
Project Administration: Samuel G. Hartharn-Evans
Resources: Samuel G. Hartharn-Evans, Magda Carr
Software: Samuel G. Hartharn-Evans, Marek Stastna

Abstract Internal Solitary Waves (ISWs) that form on internal density interfaces in the ocean are responsible for the horizontal transport and vertical mixing of heat, nutrients, and other water properties. The waves also induce fluid motion that can induce stresses and motion on floating structures, such as sea ice. This study investigates ISW-sea ice interactions. Using laboratory experiments, ISWs generated via the lock gate technique are observed interacting with weighted floats of varying sizes. The motion of these floats can be modeled effectively, simply as the average velocity of the fluid under the float, and it is found that when floats are small relative to the wavelength, they behave in the same manner as a fluid particle, but as floats become bigger relative to the wavelength, the maximum velocity decreases, and interaction time increases. This phenomenon is explained simply by the wave-induced flow as opposed to energy transfer arguments. By using this model with a large sample of theoretical waves, the float motion is parameterized based on the float length and wave parameters. Whilst small floats do not disrupt the flow patterns, the wave-induced flow under larger floats forms a pair of counter-rotating vortices at each end of the float. The formation and evolution of these flow features arise as a result of boundary layer separation with the horizontal wave-induced flow relative to the float velocity. This reveals complex dynamics due to the non-stationary behavior of both the float and flow.

Plain Language Summary Underwater waves are found in oceans across the world, including in areas with sea ice. They help mix heat, salt and other constituents in the ocean between deep and shallow waters. The Arctic is changing quickly, with summer sea ice extent declining 12.6% per decade, so we are now finding internal waves in newly ice-free areas. Experiments are used to understand how these waves interact with sea ice. It is found that bigger floats move more slowly and create more flow disturbance, albeit not enough to cause mixing. The way this flow behaves is complicated by the movement of both the model ice, and the wave. Further experimental work is needed to understand the impact of changing the thickness, concentration and shape of the ice on the behavior of these waves.

1. Introduction

Across the world's oceans, variations in seawater temperature and salinity stratify the water column, producing conditions where density disturbances can propagate as internal waves (IWs). One manifestation of these IWs are Internal Solitary Waves (ISWs). Such waves, are able to transport energy and fluid properties (such as heat, salinity, nutrients, or sediment) long distances without considerable change of form or magnitude as they exist due to a balance of nonlinear steepening and linear wave dispersion (e.g., Apel et al., 1985; Boegman & Stastna, 2019). Typically, ISWs are generated on density interfaces in stably-stratified fluids by barotropic motion over topography, internal tides interacting with localized stratification, or by nonlinear steepening of the internal tide.

The Arctic Ocean is a unique oceanographic environment for such IWs. First, the Arctic Ocean stratification is salinity-driven, with fresh, but cold water overlaying salty but warmer waters. Therefore, the mixing that can be driven by IWs is crucial for the heat distribution across the Arctic Ocean. Second, poleward of the critical latitude (which for the M2 tide is much of the central Arctic), linear internal tides are unable to propagate (Rippeth et al., 2017; Vlasenko et al., 2003), and as a result, short-scale (including nonlinear/solitary) IWs are proposed as being a key agent for the transfer of energy from tidal to turbulent scales (Rippeth et al., 2017). Finally, the presence of an ever-changing sea ice cap across most of the ocean modulates exchange of heat and momentum with the atmosphere. In some cases, this acts as a cap, preventing wind energy being converted to surface and IWs. In other cases, the motion of the ice relative to the surface waters can also act as a generation mechanism for IWs in itself (Martin et al., 2014; Zhang, Li, et al., 2022). Despite the presence of sea ice being assumed to be at least partially responsible for the low IW energy in the Arctic (due to a combination of reducing energy input, and

Supervision: Magda Carr, Marek Stastna
Validation: Samuel G. Hartharn-Evans
Visualization: Samuel G. Hartharn-Evans
Writing – original draft: Samuel G. Hartharn-Evans, Magda Carr
Writing – review & editing: Samuel G. Hartharn-Evans, Magda Carr, Marek Stastna

damping of IWs), recent studies have not found evidence of a significant rise in IW energy in response to rapidly declining sea ice extent (Guthrie et al., 2013; Guthrie & Morison, 2021).

Remote sensing (SAR imagery) of ISWs at high latitudes has confirmed the prevalence of these features in ice-free regions (Kozlov et al., 2017; Zimin et al., 2016). The retreat of sea ice over past decades allows these studies to highlight their prevalence in the presence of ice. Recently, direct observations have confirmed properties of these ISWs in proximity to the ice edge, with onshore propagating ISWs of 20–30 m amplitude, up to a maximum of 50 m (Marchenko et al., 2021), and field-scale numerical modeling has provided further details of their behavior (Kurkina & Talipova, 2011; Morozov & Pisarev, 2002). Such nonlinear IWs are thought to be formed from internal lee waves, a mechanism where the barotropic tide over topography forms steep IWs with strong nonlinearity able to overcome the rotational damping effects that prevent linear internal tide propagation at the high latitudes (Guthrie & Morison, 2021; Rippeth et al., 2017; Urbancic et al., 2022; Vlasenko et al., 2003). Upon encountering sea ice, the evolution of IWs under ice has been shown in direct observations to be dependent on ice concentration, roughness, and the stratification (Cole et al., 2018).

The ongoing declines in sea ice thickness provide a positive ice–ocean-heat feedback (Polyakov et al., 2020). By increasing the rate of atmospheric momentum flux into the ocean, and in turn inducing IW-driven mixing, the heat content of the upper ocean may increase, melting more ice, and further increasing the mixing and melting. Many observational studies have linked ISWs in the Arctic to mixing processes (e.g., Fer et al., 2020; Rippeth et al., 2017), however, there has so far been little identification of the processes that lead to this conversion of energy between the ISW interactions with ice and mixing.

As well as driving mixing, ISWs have long been known to be an agent for mass transport in the ocean. Lamb (1997) used weakly nonlinear ISW models to analyze how small particles ($L_f \ll \lambda$, where L_f is float length, and λ is wavelength) at the surface would be transported by ISWs. At larger scales relevant to sea ice, horizontal gradients in ISW-induced vertical velocity has been observed causing the flexure of sea ice in the field (Czipott et al., 1991; Marchenko et al., 2010) and the ice banding effect in the marginal ice zone has also been theoretically attributed to IW activity (Muench et al., 1983; Saiki & Mitsudera, 2016). This indicates that ISWs are capable of inducing movement of sea ice on the order of the ice floe length scales, and here, laboratory experiments are used alongside fully nonlinear models to investigate both small and much larger floating structures.

Whilst there has been considerable attention to the interaction of surface ocean waves interacting with sea ice (e.g., Li et al., 2015; Squire, 2020; Squire & Moore, 1980), relatively little is understood about the interactions of IWs and sea ice. Theoretical understanding of the evolution of internal (solitary) waves propagating beneath sea ice have primarily generalized the problem to a two-fluid problem under a flexible elastic sheet (e.g., Z. Wang et al., 2014). Such analytical studies can provide valuable insight of expected behaviors, such as changes to the wave form at low computational or experimental cost. However, field observations show the problem as more complex, with Pinkel (2005) showing the attenuation of IWs through scatter and dissipation under ice due to under-ice topography, bringing about instabilities formed from the interactions. To properly model these, numerical modeling or experiments are required, of which there have only been two process-scale studies. Carr, Sutherland, et al. (2019) conducted experiments with different surface ice types, identifying not only considerable turbulent kinetic energy dissipation at the ice-fluid interface, but also finding interaction with the ice edge can cause the ISW to break or even be destroyed by the process. Meanwhile, Zhang, Li, et al. (2022) and Zhang, Xu, et al. (2022) used numerical simulations to investigate the impact of a fixed ice keel on IW propagation and generation respectively.

Therefore, here the interrelationship between ISW-induced flow and freely floating bodies representing sea ice at the surface is explored. Whilst the work is focused on sea ice, the effects of ISW-induced currents at the surface (and therefore the phenomena identified in this study) are also of interest for SAR (synthetic aperture radar) imagery (Jackson et al., 2013), ship motion (e.g., the dead water effect (Ekman, 1904; Nansen, 1897)), oil rigs (Osborne et al., 1978), and floating offshore wind farms (Dorrell et al., 2022).

In Section 2 the experimental methodology is presented, first the laboratory methods (Section 2.1), and the quantification of the flow and float motion (Section 2.2), followed by the formulation of a Float Motion Model (FMM) for the motion of a float under ISW-induced flow (Section 2.3). The results are presented in two parts, Section 3.1 presents how the floats move under the influence of an ISW, including comparisons with the FMM and relationships between float motion and known parameters; and is followed by Section 3.2 on how the flow is changed by the presence of floats. A discussion of these results follows in Section 4.

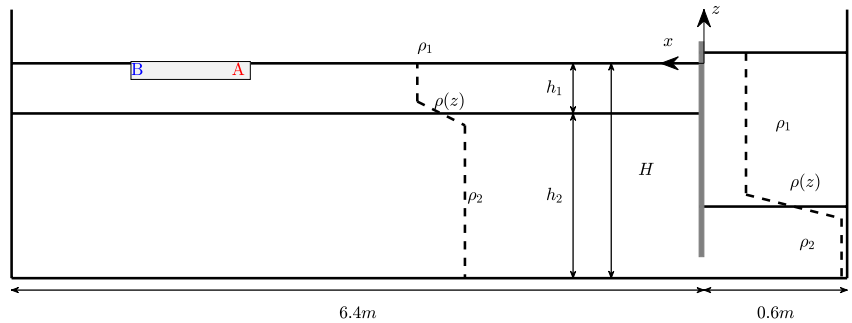

Figure 1. Schematic diagram of laboratory experiment used throughout this study, indicating the fluid densities and layer depths.

2. Methods

2.1. Laboratory Experiments

The experiments were carried out at Newcastle University in a wave tank 7 m long, 0.4 m wide and 0.6 m high, described within a Cartesian coordinate system (x, y, z) (hereafter the World Coordinate System [WCS]). The x and z directions denote the horizontal direction of wave propagation (from right to left) and vertical direction against gravity, respectively. A removable vertical gate was situated 0.6 m from one end of the flume, separating it into two sections (see Figure 1). This gate when inserted sat 0.03 m from the base of the tank, at the WCS origin $x = 0$, separating the main flume ($x > 0$) and the wave generating region ($x < 0$). $z = 0$ was at the surface of the water column (as indicated in Figure 1).

The background stratification of the main part of the flume consisted of two homogeneous layers of miscible brine solution, separated by a thin layer (known as the pycnocline) in which the density varied linearly with depth. The lower layer was a homogeneous layer of prescribed density $\rho_2 = 1{,}049.5 \pm 0.5$ kg m^{-3} with a target depth (once the tank was fully filled) of $h_2 = 0.23$ m, whilst the upper layer was a homogeneous layer of density $\rho_1 = 1{,}029 \pm 1$ kg m^{-3}, and target thickness of $h_1 = 0.07$ m (such that $\Delta\rho = \rho_2 - \rho_1 = 20 \pm 1$ kg m^{-3} in all cases). Due to practical constraints, the densities ρ_2 and ρ_1 differed slightly from prescribed values between runs, but the values were measured before the initiation of each run using a hydrometer. This stratification was set up through the initial filling of the lower layer with ρ_2 density brine, and filling the top layer using a floating sponge system. Brine was slowly drained from a reservoir above the tank through an array of sponges to ensure laminar flow into the main tank, and therefore prevent mixing into the lower layer. The tank was filled to a prescribed depth in this manner.

Once filled, the density profile of the main tank was measured using high precision micro-conductivity probes (Munro & Davies, 2006), from which the depths of each layer could be identified. The surface and bottom densities were fixed to match the measurements of the lower layer and head reservoir, respectively (see Carr et al., 2015 for further details). These sensors were moved vertically through the water column and measurements taken at 1 cm intervals, and at 0.5 cm intervals close to the pycnocline. Density profiles were measured for the downcast only. A hyperbolic tangent profile was fitted to the laboratory measurements as follows:

$$\rho(z) = \rho_2 + \frac{\Delta\rho}{2}\left(1 - \tanh\left(\frac{z + z_{\text{pyc}}}{h_{\text{pyc}}}\right)\right), \tag{1}$$

where z_{pyc} is the distance of the center of the pycnocline measured from the surface, and h_{pyc} the pycnocline half thickness. For these experiments, measured z_{pyc} and h_{pyc} were 0.068 ± 0.01 m and 0.01 ± 0.006 m respectively.

Polystyrene floats, with lead weights embedded such that their density matched that of sea ice ($\rho_f = 910 \pm 6$ kg m^{-3}), were added to the surface of the water at around $x = 3.5 - 5$ m. This location was chosen to allow visualization of the interactions of the ice and wave fully, prior to any interaction with the end wall, whilst also far enough from the gate that waves have passed through their sorting distance. Previous experiments of Carr, Sutherland, et al. (2019), in which real ice was used in a similar laboratory setting, have shown that the dominant properties of the ISW-ice interactions were due to the flow-structure interactions, rather than the material properties of the ice

Table 1
Table of Experimental Parameters for Experiments Presented in This Paper, Showing Experiment Name, Float Length, L_f, Wave Amplitude, a, Initial Wave Generating Volume, V, Float Shape, Wavelength, λ, and Wave Propagation Speed, c

Experiment name	L_f (m)	Shape	a (m)	V (L)	λ (m)	c (m s^{-1})
100mm_Circ_20L	0.10	Circle	0.053	20	1.63 ± 0.08	0.118
100mm_Circ_30L	0.10	Circle	0.065	30	1.99 ± 0.08	0.128
100mm_Circ_40L	0.10	Circle	0.074	40	2.54 ± 0.03	0.125
150mm_Circ_20L	0.15	Circle	0.053	20	1.60 ± 0.13	0.113
150mm_Circ_30L	0.15	Circle	0.079	30	2.41 ± 0.46	0.130
150mm_Circ_40L	0.15	Circle	0.077	40	3.07 ± 0.50	0.111
350mm_Squ_10L	0.35	Square	0.031	10	1.55 ± 0.13	0.120
350mm_Squ_20L	0.35	Square	0.052	20	1.61 ± 0.06	0.107
350mm_Squ_30L	0.35	Square	0.072	30	2.12 ± 0.24	0.106
350mm_Squ_40L	0.35	Square	0.070	40	2.24 ± 0.08	0.114
2.4m_Rect_20L	2.40	Rectangle	0.053	20	1.67 ± 0.05	0.137
2.4m_Rect_40L	2.40	Rectangle	0.079	40	2.61 ± 0.05	0.131
1.2m_Rect_20L	1.20	Rectangle	0.052	20	1.65 ± 0.26	0.128
1.2m_Rect_40L	1.20	Rectangle	0.070	40	2.51 ± 0.49	0.136
350mm_Squ_20L_Rounded	0.35	Square	0.036	20	1.65 ± 0.07	0.140
350mm_Squ_30L_Rounded	0.35	Square	0.068	30	2.00 ± 0.21	0.115

(such as temperature or elasticity). Hence weighted floats are deemed an appropriate substitute for real ice in this study. Two reference locations A and B are identified at the right and left ends of the float respectively (Figure 1), which are used to aid explanation of the dynamics later in the results.

To generate a mode-1 ISW, the gate was inserted at $x = 0$ m, and through a single sponge behind the gate, a further volume of ρ_1 density brine added, causing a downwards displacement of the pycnocline behind the gate. The volume of brine added behind the gate was varied to alter wave amplitude, and was determined by the change in total fluid depth, measured before and after filling behind the gate. The total fluid depth after filling behind the gate was fixed at $H = 0.3$ m throughout the study. Whilst the generating volume, V is reported in Table 1 as an indicative measure of wave size, it should be noted that the relationship between V and amplitude is not linear, in particular at very large amplitudes the wave passes the conjugate limit and further increases in volume manifest only as broadening of the wave (Grue et al., 2000; Lamb & Wan, 1998; Lamb & Warn-Varnas, 2015; Turner & Vanden-Broeck, 1988).

The experiment was initiated by the vertical removal of the gate, which by producing a discontinuity and displacement of the pycnocline resulted in the generation of a mode-1 ISW. To enable the transition from ice-free to ice-covered waters, these experiments were performed without a lid, and therefore much of the tank had a free surface. A total of 50 experiments were performed, 16 of which are presented here with differing combinations of float sizes and wave generating volumes, summarized in Table 1. Due to practical considerations, the shape of float was different for $L_f > 0.15$ m (where floats were rectangular) than for floats $L_f \leq 0.15$ m (where floats were circular).

2.2. Flow and Float Quantification

Fluid motion was viewed through the movement of light-reflecting neutrally-buoyant tracer particles within a vertical light sheet. These tracer particles were made of inert "pliolite" 150–300 μm in diameter, and had neutral buoyancy over the density range throughout the water column. A vertical section in the mid-plane of the tank was illuminated by a continuous collimated light sheet from an array of light boxes placed beneath the transparent base of the tank. Fixed digital video cameras recorded the particle motions within the light sheet. The cameras (UNIQ UP-1830CL-12B) were set up outside the tank, synchronized in time and positioned to have overlapping fields of view. They were centered in the vertical direction on the pycnocline to avoid distortion and

perspective errors in the upper layer (including the pycnocline and float interactions). The cameras recorded at 30 f.p.s at 1,024 × 1,024 pixels resolution. Past experiments found the settling velocities of the seeding particles to be two orders of magnitude lower than the wave induced vertical velocities (Dalziel et al., 2007). The continuous synoptic velocity (u, w), and vorticity, ω, fields, in a given two-dimensional vertical slice (x, z) of the flow were quantified using Particle Image Velocimetry (PIV) in the DigiFlow software package (Dalziel et al., 2007) using the most recent algorithm (2017a) with window size and spacing of 19 × 19, and 16 × 16 pixels squared respectively.

Wave properties were measured using the method described in Carr, Stastna, et al. (2019) (their Figure 2). The time series function of DigiFlow, which tracks changes of pixel values in a given column, row or defined line over time, was used to measure wave speed, c, and amplitudes, a. Tracing of the streamline coinciding with the pycnocline is possible through these time series due to the high concentration of seeding particles that collects at the density interface. It was not always possible to trace the exact same streamline based on height between runs, however, the closest available streamline to the pycnocline center was always chosen. To calculate c, the time at which the interface reached maximum displacement was measured from vertical time series (constructed from a given column of pixels from each frame), and the wave speed calculated from the slope of these times, and the fixed x locations at which the time series were produced. Vertical time series were also used to measure wave amplitude; the maximum displacement of a chosen streamline, with this process repeated at three vertical cross-sections in order to measure variance. Finally, wave length, λ, was measured as twice the time interval between the streamline crossing half the maximal displacement ($z = -(z_{\text{pyc}} + (a/2))$), multiplied by c. Due to the combining of measurement errors in this approach, wavelengths reported in Table 1 are an average of the measured wavelengths and Dubreil-Jacotin-Long (DJL) wavelengths, with uncertainty from the extremes of these four measurements. The DJL equation is a nonlinear, elliptic eigenvalue problem for the isopycnal displacement $\eta(x, z)$,

$$\nabla^2\eta + \frac{N^2(z-\eta)}{c^2}\eta = 0 \tag{2}$$

where $N^2(z - \eta)$ is the square of the buoyancy frequency evaluated at the height of the isopycnal far upstream $z - \eta(x, z)$ (the upstream height). The equation was solved by a pseudospectral method in a frame of reference moving with the wave $\rho(x - ct, z) = \bar{\rho}(z - \eta)$. Here $\bar{\rho}$ is the background (i.e., far upstream) density profile. Solutions were obtained using a version of the software publicly available at Dunphy (2011).

Fully non-linear DJL solutions have previously been shown to be in good agreement with laboratory waves (Luzzatto-Fegiz & Helfrich, 2014). The package was used to calculate a solution for each experiment with matching density profiles and wave amplitudes.

Dependent on the size of the floats, two techniques for visualizing float motion were used. For floats with $L_f \leq 0.15$ m, the Particle Tracking Velocimetry (PTV) function in DigiFlow (Dalziel et al., 2007) was used on videos from a downward looking camera, with the floats illuminated from above using an array of LED (light-emitting diode) lights. This algorithm was employed using a blobs policy, using blob validation parameters that matched specific float sizes and shapes.

For floats with $L_f > 0.15$ m, due to the scale of the float in relation to the cameras' field of view, the PTV method was not suitable. Instead, float location was computed using videos from the side on cameras, employing an algorithm described as follows. The lower edge of the ice floats were identified in raw images from the videos by a combination of identifying peaks in light intensity which exceeded a prescribed threshold, and where those peaks were within a depth range that the float bottom would be expected to reside. Peaks in brightness intensity are expected to be found from the reflection and scattering of the vertical light sheet on the white underside of the float. For each column of pixels, pixels above the peak in intensity were masked. Hovmoller time series (horizontal time series constructed from a given column of pixels from each frame) of the movies from a row of pixels between the bottom of the float and the surface were taken, and the edges of the floats identified as the boundary of the mask, therefore providing a location for the float edge at each time step. The center of the float (the float track) could easily then be calculated, and float velocities at each time step calculated by a Finite Differencing scheme. Whichever of these methods are used, throughout this paper the observed floats from the laboratory experiments will be referred to as (Obsv.). The float tracks from multiple cameras were collated, and smoothing was applied to remove small errors that could arise due to this collation.

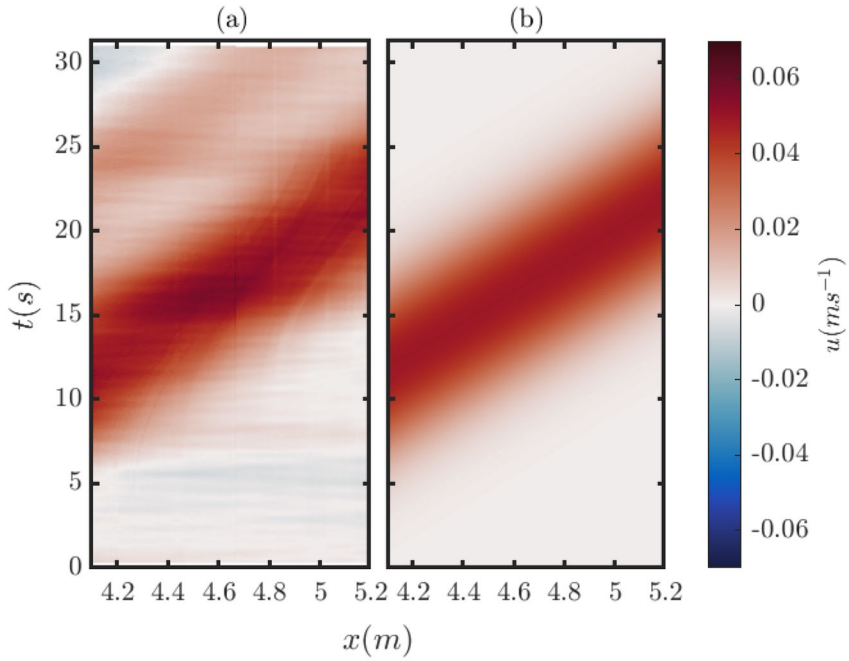

Figure 2. Hovmoller time series of the horizontal velocity for Particle Image Velocimetry laboratory measurements just below the lower surface of the floats (a) and for a Dubreil-Jacotin-Long solution at the upper surface (b), as given by Equations 4 and 5 respectively.

2.3. Float Motion Model (FMM)

In this section, a Float Motion Model (FMM) is developed and described in order to estimate float position from hydrodynamic data, whether that is theory, simulations, or measured. The robustness of the model estimate will be compared to experimental measurements in Section 3.1. The FMM assumes that the float moves at the average speed of the fluid beneath it by solving the equation:

$$\frac{dx_f}{dt} = U(t) = \frac{\iint u(x_f(t), t)\, dx\, dy}{\iint dx\, dy}, \tag{3}$$

where $x_f(t)$ is the horizontal position of the center of the float at time, t, U is the horizontal velocity of the float, and integration is performed over the spatial extent of the float. The reference surface velocity is defined as:

$$u(x, t) = u_{PIV}(x, z = z_b, t), \tag{4}$$

or

$$u(x, t) = u_{DJL}(x - ct, z = 0), \tag{5}$$

where u_{PIV} is the horizontal velocity field measured in the laboratory just beneath the base of the float ($z = z_b$) and u_{DJL} is the horizontal velocity field computed from the fully nonlinear DJL Equation 2 at the surface ($z = 0$). The DJL solution is transformed from a stationary frame of reference to a time-varying one as shown in Equation 5. There is no physical float present in the DJL model, therefore solutions of the FMM (Equation 3) with DJL velocities as input (Equation 5) provide reference states which can be compared with laboratory observations in which a float is present to assess the impact of the float on the flow. Examples of u_{PIV} and u_{DJL} are provided in Figures 2a and 2b respectively. Note that other input signals could also be employed (e.g., a numerical model).

The FMM Equation 3 is solved in the following way. Given the velocity field and float position $t = t_n$, along with the updated velocity field at $t = t_{n+1}$ the float's position, x_f, is updated using a fourth-order Runga-Kutta time integrator. The grid points containing the float at time t are identified, and an average (weighted by the width of the float at each x position) velocity is calculated where the fluid velocity is assumed to be constant in the y direction, to account for the shape of the float. The model is a version of Lamb (1997) adapted for float lengths longer than

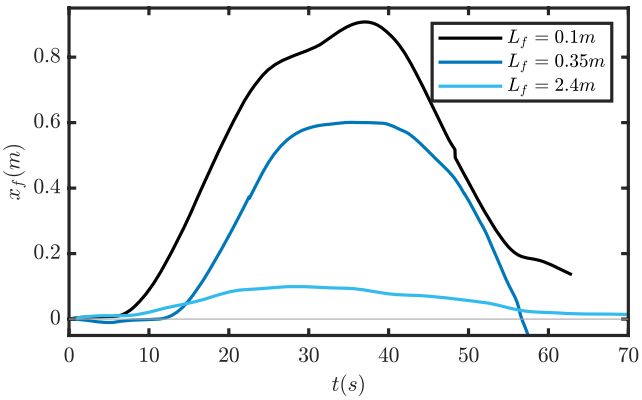

Figure 3. Time series of experimentally measured float location during the passage of an Internal Solitary Wave for three floats of varying lengths, experiments 100mm_Circ_20L, 350mm_Squ_20L and 2.4m_Rect_20L. x location is relative to the initial position of the float.

the grid spacing. Throughout, when the experimental PIV velocity, u_{PIV}, is utilized in the FMM it will be referred to as FMM/PIV, and when DJL solutions, u_{DJL}, are used it will be referred to as FMM/DJL.

3. Results

3.1. Motion of Floats

The wave-induced horizontal flow in the upper layer is oriented in the same direction as wave propagation. As the wave approaches the fluid is accelerated in the same direction as the wave reaching a maximum velocity directly above the wave trough. After this point the fluid decelerates as the wave passes (see Figure 2 for example).

Consequently, as a result of this wave-induced flow, floats (Obsv.) travel in the same horizontal direction as the wave, accelerating as the wave approaches and decelerating once it passes. The observed floats never quite reach the same speed as the wave, and so the float moves backwards in a frame of reference moving with the wave, and after passing through the mid-point of the wave, slows (in a stationary frame of reference) (Figure 3). Figure 3 shows experimentally measured float motion for three different float sizes, where the initial generating volume is held constant ($a = 0.0525 \pm 0.0005$ m), and so only the float changes (within experimental variability). In experiments, due to reflection of the wave from the end wall of the tank, the tracks of floats follow a bell shape, indicating transport of the float by the reflected wave. The bell shape seen in Figure 3 is due to the wave being reflected off the end wall of the flume and subsequently transporting the float back upstream. With increasing float length, L_f, the total travel by the float decreases, seen in the difference between the 2.4 m float, which moves 0.1 m and the 0.1 m floats, which move 0.9 m in Figure 3.

To demonstrate the efficacy of the FMM in predicting the actual motion of the float, the motion of the Observed floats is compared with the FMM applied to DJL solutions (FMM/DJL) and the FMM applied to PIV observations (FMM/PIV) in Figure 4. Positions A and B on the float are hereafter defined as the edge of the float which is first impacted by the wave, and the opposite edge respectively (Figure 1). The velocities at these points (i.e., $u(A) = u\left(x_f - \frac{L_f}{2}, t\right)$, $u(B) = u\left(x_f + \frac{L_f}{2}, t\right)$) are shown to indicate the range of fluid velocities influencing the float at any given time. The float velocity over time, as well as the fluid velocities at the endpoints of the float (A and B) are shown (Figure 4). First considering FMM/DJL, for small floats (Figure 4a), the floats essentially act like buoyant tracer particles, and the float velocity closely follows a sech^2-like profile. U peaks at almost the same height as $u(A)$ and $u(B)$. This float velocity profile is situated between the similar shaped curves at point A and point B. To explore the impact of differing float sizes and wave amplitudes, following the results of Carr, Sutherland, et al. (2019), L_f/λ is used here as a nondimensionalized float length, the full nature of this relationship will be explored later. As L_f/λ increases, the float velocity profiles undergo two changes. First, the maximum float velocity falls, and the curve widens, and by $L_f/\lambda = 1.6$ (Figure 4g), a clear flat top to the curve is present. Second, a slight asymmetry of the peak, such that the rising limb is longer than the falling limb can be observed (Figures 4d and 4g). For smaller L_f/λ, the $u(A)$ and $u(B)$ curves are broader, due to the length of interaction with the wave at these points being increased by the float moving with the wave.

The measured U, and u at points A and B from PIV (Obsv./PIV) are in good agreement with the FMM/DJL solutions, albeit with experimental noise/error (Figures 4a, 4d, and 4g compared to Figures 4b, 4e, and 4h). The changes in velocity profiles as L_f/λ increase match those for the FMM/DJL, as do the overall shapes of profiles, indicating the suitability of this model. Figures 4g and 4h show that $U_{\max}$ for the longer floats were overestimated by the FMM/DJL solutions. This discrepancy can be explained by the fact that FMM/DJL does not contain a real float, and so does not capture the flow features documented for longer floats in Section 3.2. Differences between the FMM/DJL and laboratory observations are to be expected as the float size becomes non-negligible. Some interactions with the tank side wall were observed for the longest floats, which may have further slowed the float movement. When further comparing to FMM/PIV (modeled float velocity based on PIV measurements), the signal is considerably noisier, indicative of amplification of observational error and noise by the model. However, broad patterns can still be identified as being in good agreement (Figures 4c, 4e and 4h) with both the FMM/DJL solutions, and Obsv./PIV.

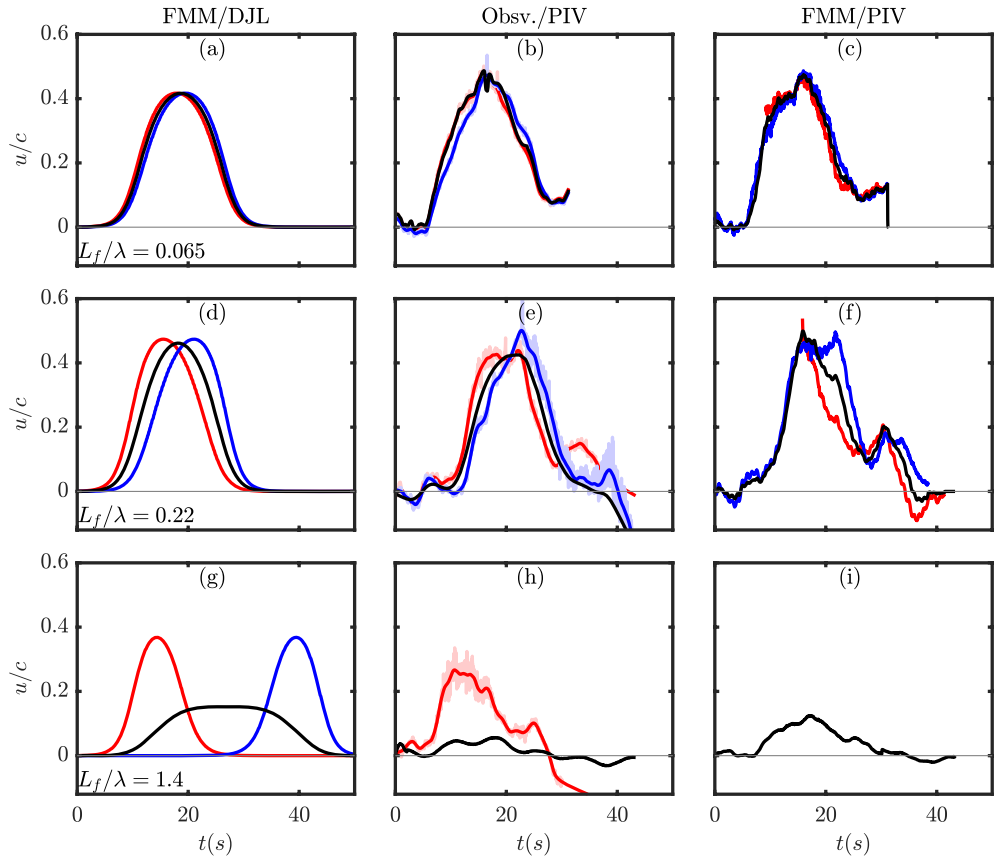

Figure 4. Time series of float velocity (black) during the passage of an internal solitary wave for three floats of varying lengths (a–c) representing $L_f = 0.1$ m, (d–f) representing $L_f = 0.35$ m and (g–i) representing $L_f = 2.4$ m, and the horizontal fluid velocity at points A (red) and B (blue) on the float. Note that the y axis label u/c is actually U/c for all black traces. Left column (a, d, g) shows the Float Motion Model (FMM) applied to Dubreil-Jacotin-Long (DJL) velocity data, the central column (b, e, h) shows the observed float motion, and right column (c, f, i) showing the FMM applied to observed Particle Image Velocimetry (PIV) velocities. All velocities normalized by the internal wave propagation speed, c, and smoothed PIV velocities shown in the central column (smoothed lines in dark colors, faded colors the original).

Any interactions between the float and the flow will also be reflected in those models, in a way that DJL cannot reflect. Note that for the largest floats, the width of the experimental viewing window is insufficient to measure $u(B)$. These results show that a DJL wave applied to the model (FMM/DJL) gives a good understanding of float motion, despite no real float being present in the model. The good agreement between FMM/DJL and laboratory float motions indicate that the background ISW-induced flow is the main parameter controlling the float transport.

Figure 5 are a representation of the FMM, showing distribution of wave-induced velocities influencing a float for each timestep, explaining observed behaviors. For small floats (Figure 5a), the range of wave-induced velocities being experienced by a float at a given time are small, and as a result U closely matches the motion of fluid parcels, similar to Lamb (1997). As the float size increases, at any given time, the float is under the influence of fluid traveling at a range of spatially varying wave-induced velocities. This results in the float propagation speed being slower than the maximum wave-induced fluid velocity, influenced by the fluid either side of the wave center, which has lower velocities. Extended yet further, once $L_f \gg \lambda$ (Figure 5c), the entire wave can be under the float, and much of the float is influenced by the non-moving fluid (the probability density function is dominated by $u/c = 0$). As a result U (as the average of this distribution) is much slower than the fastest wave-induced fluid speeds (e.g., the red and blue lines), and interaction time increases. This model therefore explains the relationship of faster U_{max} with smaller values of L_f/λ.

Given the good agreement between the FMM/DJL model and the laboratory observations, the relationship between float size, wave size and the motion of the float can be explored using FMM/DJL. Figure 6a shows the relationship between float length, L_f, and maximum float velocity, U_{max}, for a small ($a = 0.0351$ m) DJL wave.

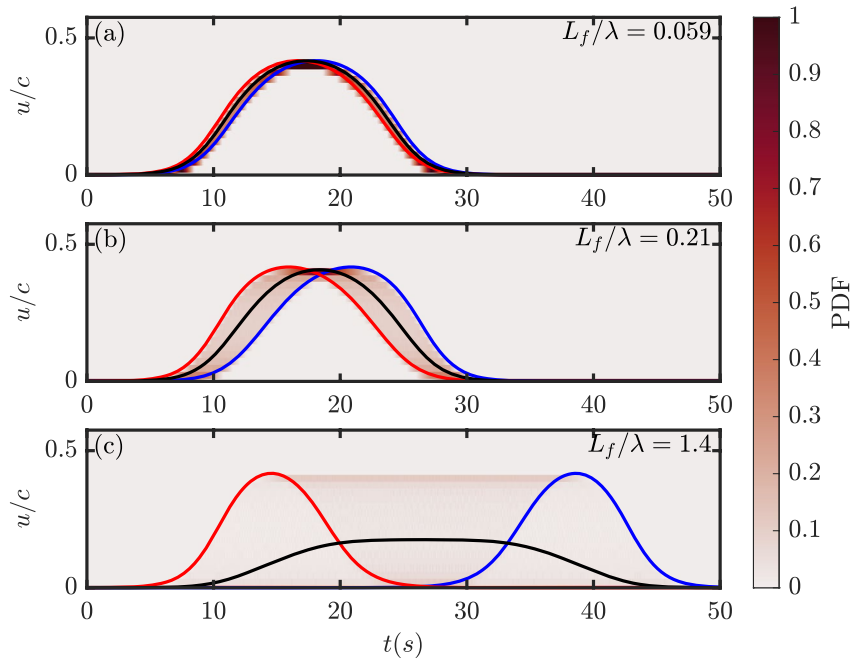

Figure 5. Histogram time series of fluid velocities between Point A (red trace) and Point B (blue trace) (i.e., under the float) for the Float Motion Model (FMM) applied to Dubreil-Jacotin-Long (DJL) waves (FMM/DJL), showing the probability density function (PDF) of fluid velocity. The same DJL wave is used for each simulation, with only float size varying from $L_f = 0.1$ m (a), $L_f = 0.35$ m (b) and $L_f = 2.4$ m (c). All velocities normalized by the internal wave propagation speed, c.

Figure 5a shows that $U_{max}/c \propto \text{sech}^2(L_f)$, and maximum float speed decreases with increasing float length, this sech^2 relationship arising entirely empirically. The effect of increasing the wave amplitude, a, is to increase the maximum float speed, although the effect is stronger for a very small float ($L_f = 0.1$ m, Figure 6b, blue line) than for larger floats (red line, Figure 6b). To capture these behaviors, a parameterization of the wave-induced float motion is captured by the following relationship:

$$\frac{U_{\max}}{c} = \left(b_0 \frac{a}{H} + b_1\right)\left(\text{sech}^2\left(\frac{L_f}{b_2\lambda + b_3}\right) + b_4\right) \tag{6}$$

where $b_0 = 1.2458$, $b_1 = 0.1538$, $b_2 = 0.6681$, $b_3 = -0.1870$, and $b_4 = 0.2233$, are calculated empirically. The goodness of fit measure between this parameterization and observations is $R^2 = 0.9969$ when ($n = 2{,}940$) FMM/DJL solutions are used, and $R^2 = 0.8579$ when Obsv./PIV measures are utilized (Figure 6c). Given the large uncertainty in some experimental wavelengths (Table 1), this is still a particularly good result.

3.2. Observations of Float Interactions With Internal Wave-Induced Flow

For smaller floats, flow does not deviate from the baseline of an ISW with no floats. However, as floats become larger (observed for $L_f \geq 0.35$ m), they begin to interact with the flow, resulting in new flow features being seen. In particular, when the float accelerates as the ISW approaches, a separation bubble, evolving into a clockwise vortex forms attached to the float at point A (Figures 7a–7d, blue region of vorticity). As the float starts to move, a jet initially forms down under the float at point B (Figures 7b and 7g, red region of vorticity), which as the float speed increases, evolves into a counter-clockwise vortex at point B (Figure 7c, red region of vorticity). As the mid-point of the wave passes point A, the vortex there stagnates and declines (Figures 7d and 7e). Once the mid-point of the wave passes point B, the float begins to slow, and the vortex at point B detaches from the float, initially forming a vortex of opposite polarity in the lee of the float (Figure 7d, blue vorticity). Then, as the wave continues to overtake the float, the vortex is transported in the same direction as the wave (Figure 7e). At larger wave amplitudes (Figures 7f–7j), the size of these vortex structures increase. Additionally, the clockwise vortex formed at point A is advected forward under the float, whilst remaining attached (in positive x direction, Figures 7h and 7i). An additional vortex forms at point A again.

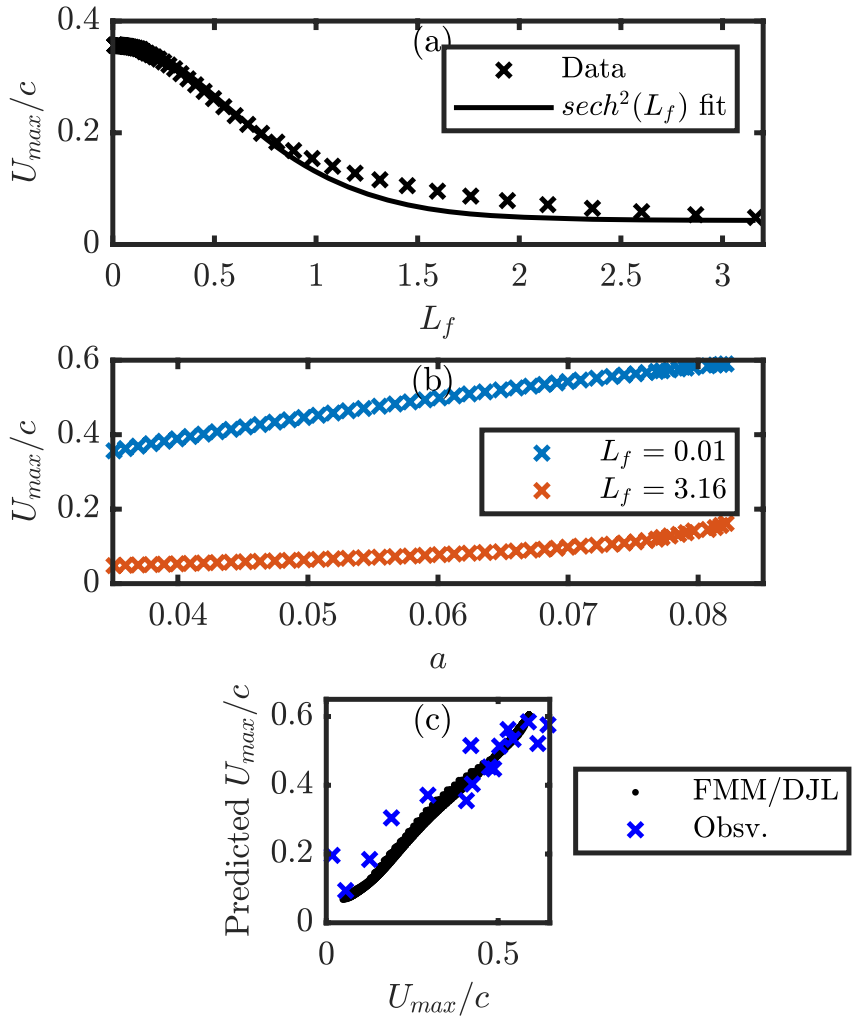

Figure 6. Indicative illustrations of the relationship between (a) float length, L_f, and maximum float speed, U_{max}/c, from Float Motion Model (FMM) applied to Dubreil-Jacotin-Long (DJL) waves (FMM/DJL), (b) wave amplitude, a, and U_{max}/c, and (c) goodness of fit of Equation 6 to observations for the FMM/DJL (black dots) and direct measurements from the laboratory experiments (blue x), with R^2 indicated for the FMM/DJL solution.

At larger L_f (Figure 8), the overall structures formed in the flow are the same, but at point A there is a further tendency for the vortices to be transported upstream (Figures 8c and 8d), and for multiple clockwise vortices to be formed along the base of the float (indicated by black arrows in Figures 8c, 8d, and 8g). Due to the length of the float, features at B were not visualized, but were observed to resemble those for smaller L_f floats.

To investigate the role of the shape of the float edge on these dynamics, a pair of experiments:

350mm_Squ_20L_Rounded and 350mm_Squ_30L_Rounded were carried out with a rounded edge to the floats (Figure 9). For the larger wave, a similar set of dynamics are observed to the comparable experiment with a sharp corner, but the vortex formed at A was smaller (Figure 9h). Whilst the jet forms at B, no vortex forms here (Figure 9h). The smaller wave extends this trend further, with no vortex forming at A either (Figures 9b and 9c), although the other similar flow features continue to evolve in a similar manner, including the formation of a small detached vortex at point B as the wave passes (Figure 9d).

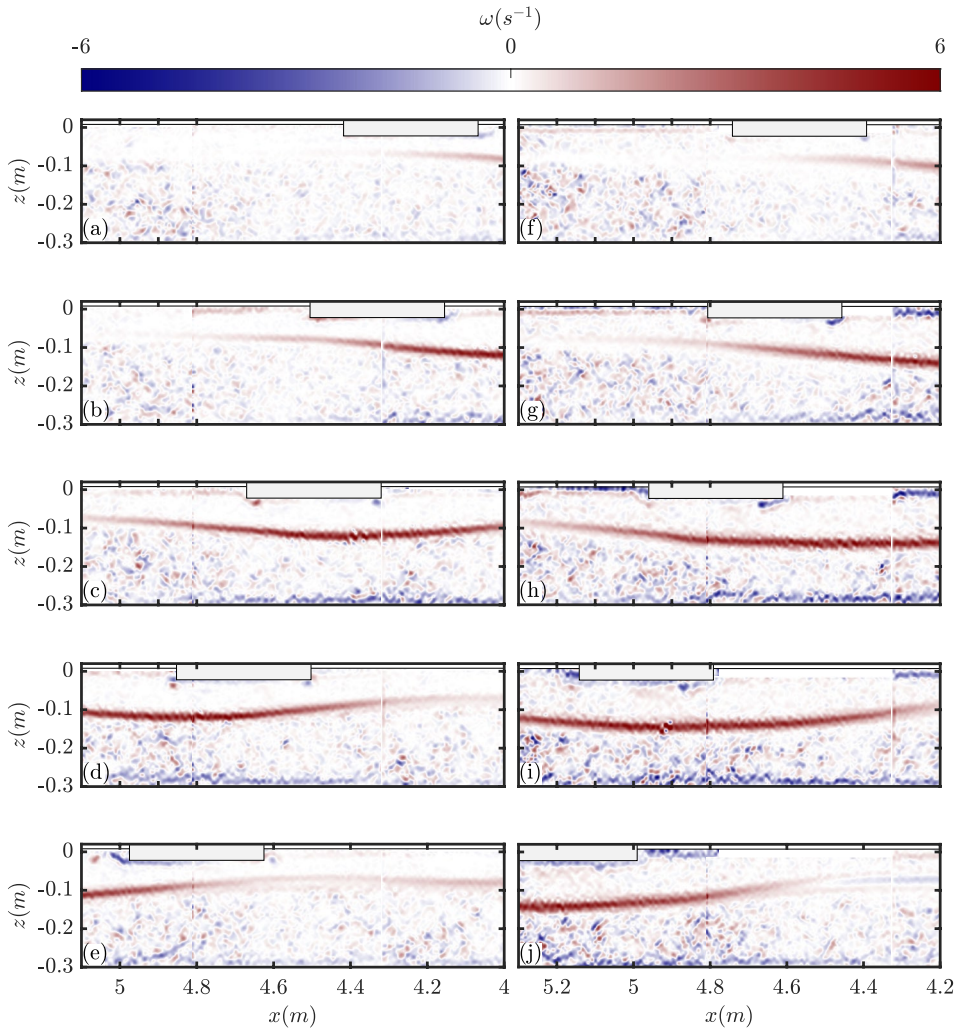

Figure 7. Time sequences showing medium float experiments for a small amplitude wave (350mm_squ_20L, left) and large amplitude wave (350mm_squ_40L, right). The color scheme displays vorticity. The observed location of the float is overlaid to aid visualization. Time interval between images is $\Delta t = 4$ s. Note that images are made up of images from three cameras merged to form a single image. Corresponding movies of the experiments (Movies S1 and S2) are provided for additional clarity.

4. Discussion

4.1. Application of Theory to Understand the Flow and Floats

The motion of the floats is here modeled using a simple model, which, without using energetic arguments, assumes the float moves at the average velocity of the fluid in contact with the float. The model gives strong agreement with past work (e.g., Carr, Sutherland, et al., 2019), and with experimental results presented here, and so can further be used to understand the patterns of flows described in Section 3.1. Past work has applied a full calculation of the forces invoked on floating structures under the influence of ISWs through an adapted Morison formula (e.g., Song et al., 2011; X. Wang et al., 2018), but such complexity has not been necessary here, providing a more intuitive result for the motion pattern of ice, and similar floating bodies. Intuitively, the result of larger floats traveling less fast would appear to be due to the increased mass relative to the wave, and to reach the same speeds the force exerted on the float by the wave would need to increase accordingly. However, the good fit between the FMM (which does not take into account these forces, or any energy transfer) and laboratory observations indicates that this relationship is in fact a more simple outcome of the basic behavior of the ISW-induced flow, and increasing influence of the still water either side of the wave as float size increases. Estimating the

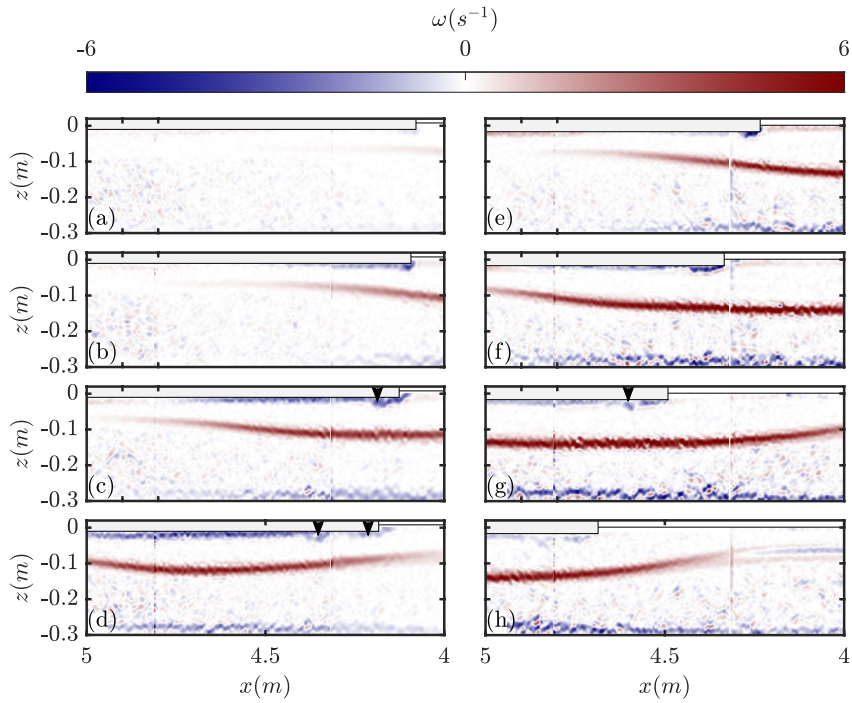

Figure 8. Time sequences as in Figure 7, but showing long float experiments for a small amplitude wave (1.2m_rect_20L, left) and large amplitude wave (1.2m_rect_40L, right). Time interval between images is $\Delta t = 4$ s. Corresponding movies of the experiments (Movies S3 and S4) are provided for additional clarity.

efficiency of energy transfer between the wave's Available Energy (AE) and float's maximum Kinetic Energy (KE_f, at the point at which $U = U_{\max}$) as:

$$KE_f = 0.5 M_f U_{\max}^2, \tag{7}$$

$$AE = APE_{DJL} + KE_{DJL} \tag{8}$$

where M_f is the mass of the float, $U_{\max}$ is taken from experimental observations, APE_{DJL} and $KE_{DJL} = u^2 + v^2$ are the estimates of Available Potential Energy and Kinetic Energy from the DJL solution of the experimental waves. The efficiency of transfer is defined to be KE_f/AE. Over all experiments studied the maximum efficiency of energy transfer was between 0.06% and 2.8%, indicating the float takes a very small proportion of the AE from the wave system in each case. The efficiency in energy transfer was seen to increase slightly as float size increased.

To understand the features observed in Section 3.2, the vortex features formed by the ISW-ice interaction are here discussed in the context of boundary layer flows, and specifically theory developed for elongated bluff body aerodynamics (e.g., Aleyasin et al., 2021; van der Kindere & Ganapathisubramani, 2018). To understand such features, it is the velocity relative to the boundary layer that matters. Usually in IW studies, a fixed boundary layer means this is simply the flow field in a fixed frame of reference, but in this case it is valuable to consider the boundary layer flow using an adjusted horizontal velocity, so that the PIV velocities of wave-induced flow relative to the float's measured motion are considered.

In a stationary reference frame, the initial formation of the vortex at point A can be understood as a separation bubble and instability resulting from the reverse flow, similar to Aleyasin et al. (2021) (their Figure 5e). At point A, as the wave approaches, a flow in the same direction as the wave is found in the upper layer (Figures 10a and 10b). As the flow approaches point A, it decelerates due to the obstacle, and stagnates. This deflects and concentrates the flow under the float, such that there forms a separation bubble (Figures 10c and 10d). A similar vortex feature was previously observed in an ISW context by Talipova et al. (2013) (their Figure 8) over a fixed step, but the formation and evolution was not discussed in detail.

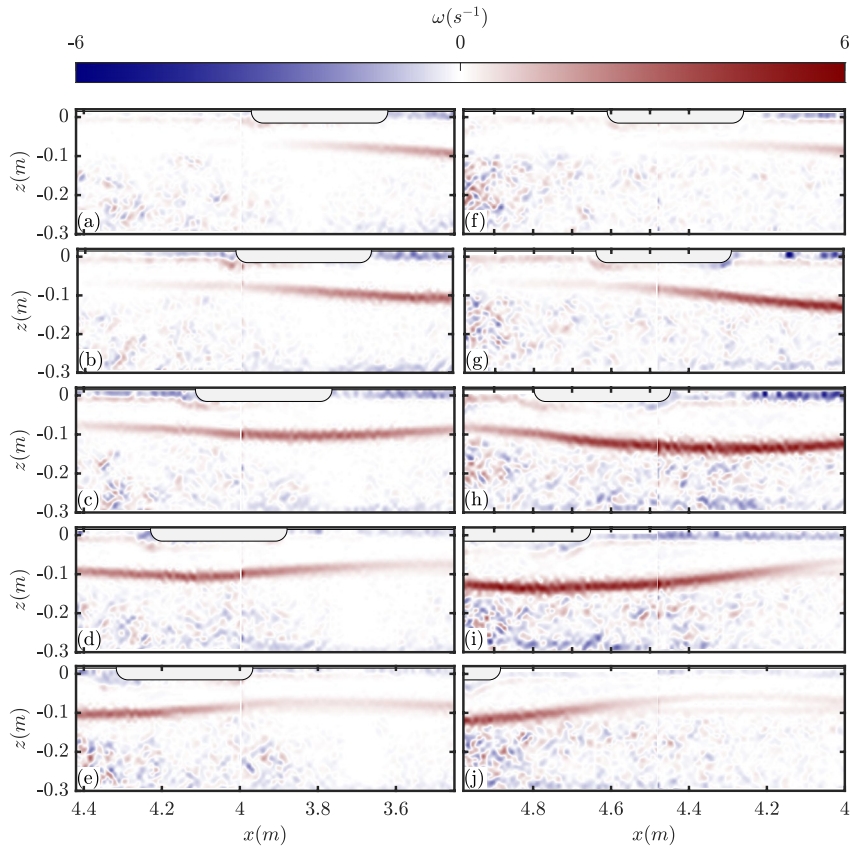

Figure 9. Time sequences as in Figure 7, but showing curved float experiments for a small amplitude wave (350mm_squ_20L_C, left) and large amplitude wave (350mm_squ_30L_C, right). Time interval between images is $\Delta t = 2.8$ and 4 s for the left and right sides, respectively. Corresponding movies of the experiments (Movies S5 and S6) are provided for additional clarity.

However, the vortex at point B forms whilst the velocity (in a stationary reference frame) is approximately equal to zero (Figure 10a). When the reference frame of the float is considered ($u - U$), the horizontal velocity becomes negative at point B (Figure 10b). This builds up a region of pressure ahead of point B, which manifests as a jet of fluid toward $x = 0$. Simultaneously at point A, the flow velocity induced by the wave is always faster than the floats ($u - U > 0$), causing a deceleration and stagnation of the flow behind the float (Figure 10h, as seen in the non-adjusted flow). As a result, there is deflection of the flow below the float, producing a separated and recirculating region at the corner, manifesting as a vortex with opposite vorticity to the surrounding fluid. By the point the wave is mid-way across the float, $u - U > 0$, and the vortex at B is advected, leading to an attached vortex in the lee of the float (Figure 10h), similar to Aleyasin et al. (2021) (their Figures 5a, 5c, and 5e).

As the float continues to travel at $U < c$ the wave begins to overtake the float, during which process, the vortices at points A and B persist (Figure 10f), before $u(A) - U$ approaches 0 (as U reaches $U_{\max}$, and u decreases at the tail of the wave), and the flow becomes unfavorable for the vortex. Simultaneously, the vortex at point B are shed toward positive x, since $u(B) - U > 0$. The presence of these features has the effect of reducing the wave-induced velocities at the wave-float interface, and therefore also the float velocity, as seen by the difference between both $u(A)$ and U in Figures 4g and 4h.

The identification here of a relationship between L_f, λ, and a (Equation 6) further simplifies the understanding of the motion induced by ISWs. However, the surprising result that this relationship takes the sech^2 form is as yet unexplained.

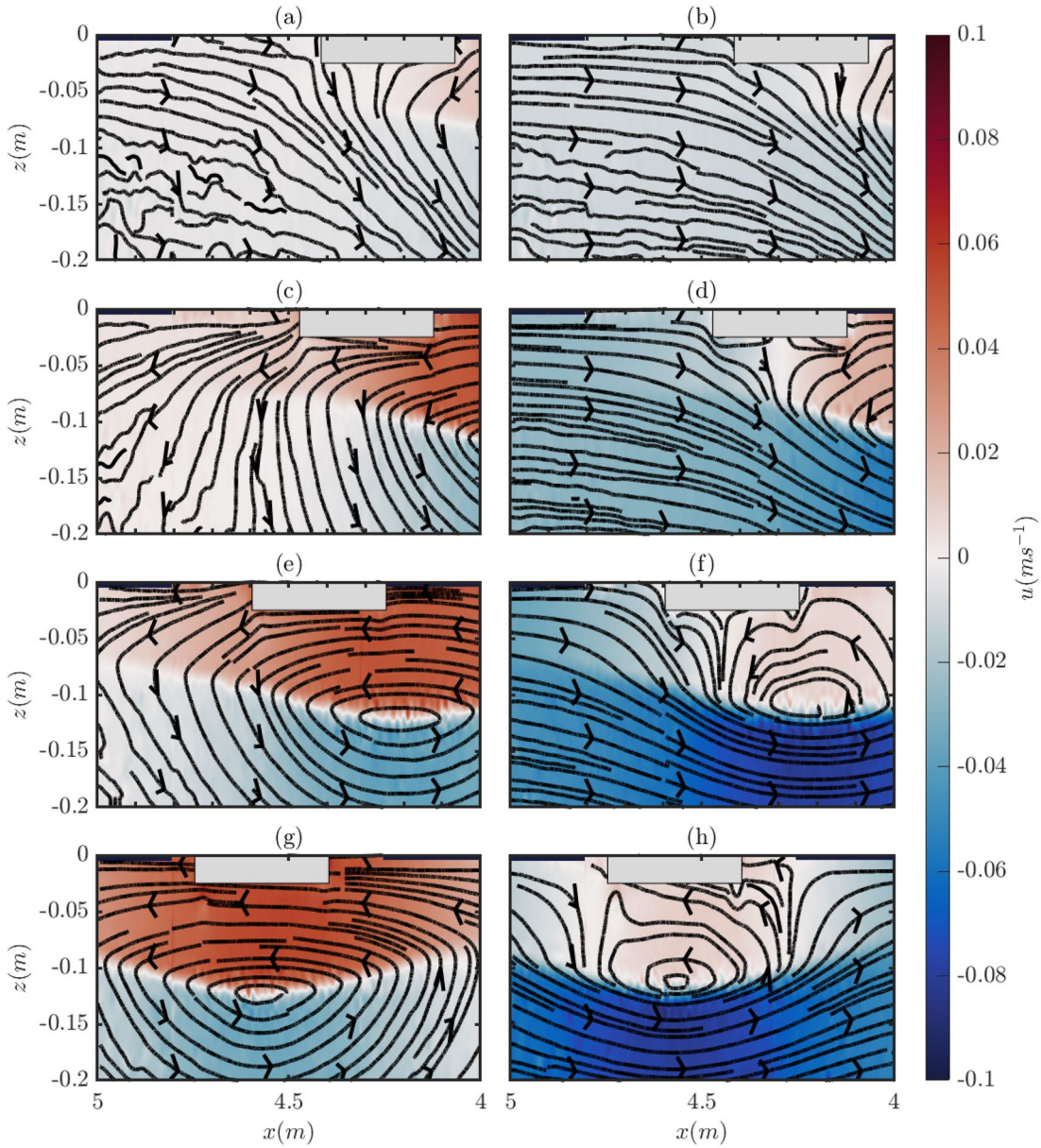

Figure 10. Time sequences showing the medium float experiment 0.35m_squ_20L, for a stationary frame of reference (left) and a frame of reference relative to the float velocity (right). The color scheme displays horizontal velocity, and overlaid are streamlines. The location of the float is indicated. Note that images are made up of images from three cameras merged to form a single image.

4.2. Field Scale

Past studies on the interactions between waves and ice have indicated the ratio between L_f and λ is critical for understanding the different flow regimes involved for example, Bennetts and Williams (2015) and Carr, Sutherland, et al. (2019) for surface and IWs, respectively. Therefore, the overall approach here to scaling to the field scale is studying the ISW-ice interactions at a complete range of ratios of L_f/λ. Figure 4 indicates the success in moving through a range of regimes, implying results are applicable to float sizes of all scales studied, with the expectation that these trends will continue as L_f becomes very small or large.

Following Bennetts et al. (2015), Bennetts and Williams (2015), and Timco (1980), the density difference between the floats and surface fluid is comparable to that in the field, which allows the results to be scaled effectively between laboratory and field scales. Whilst the surface fluid density was chosen primarily to optimize

visualization with the pliolite seeding, this also coincided with the surface water density of the ocean, so that both the surface and float densities also match those in the field.

Various other scales can be applied to scale flows, the most commonly used are the Reynolds number, $\mathrm{Re} = UL/\nu = cH/\nu$ where U, L are indicative velocity (not float velocity as elsewhere in this paper) and length scales, here taken to be c and H respectively (formulation from Hartharn-Evans et al., 2022). The Froude number, $\mathrm{Fr} = U/\sqrt{gL}$ is also a useful scaling term. Assuming $\nu = 10^6\ \mathrm{m^2\ s^{-1}}$, typical values for the field are $\mathrm{Re} \approx 10^6$–10^8 and $\mathrm{Fr} \approx 0.001$–$0.01$. Typical values for these experiments are $\mathrm{Re} \approx 3 \times 10^4$ and $\mathrm{Fr} \approx 0.06$. The density of the fluid in the bottom layer ($\rho_2 = 1{,}049\ \mathrm{kg\ m^{-3}}$) was chosen to make $\Delta\rho$ as large as practically possible. The impact of a higher $\Delta\rho$ in these experiments is to increase the wave speed, acting to counter the effect of smaller length scales in the wave speed, and therefore Froude number. Differences in Re are unavoidable at these small scales, but are in line with previous laboratory studies.

4.3. Roughness and Shape of Floats

Experimentally, sweeping all possible parameters related to this interaction problem is practically not possible, but existing literature can indicate how the interactions may occur for other parameters.

The flow features induced by the presence of floats in an ISW are a special case of flow over elongated bluff bodies, a phenomenon well studied due to its engineering applications (e.g., Aleyasin et al., 2021; van der Kindere & Ganapathisubramani, 2018). However, spatio-temporally varying flow and motion of the float complicate the situation in comparison to a fixed body in constant flow. Such studies identify the edge roundness of the body as a key factor in the formation of vortices associated with separation, and for this reason a pair of experiments were carried out with rounded edges. Whilst some reduction in the strength and extent of these features was identified (most notably in the smaller wave experiment), the pair of counter-rotating vortices at each end of the float could still be formed, albeit at larger wave amplitudes than for a sharp corner.

An aspect of the interaction of particular oceanographic interest is diapycnal mixing induced by the interaction. Here this is not measured, due to experimental difficulties in doing so. Past results of Carr, Sutherland, et al. (2019) are indicative of enhanced Turbulent Kinetic Energy dissipation at the ice-water interface, associated with the ISW-ice interaction, indicating enhanced energy loss from the wave due to the interaction, but not necessarily diaypycnal mixing. However, in that study, the formation of Kelvin-Helmholtz (K-H) instability on the pycnocline in experiments with a deep ice in comparison to the pycnocline depth were indicative of enhanced diapycnal mixing in that case. Although the vortex features in these experiments at times reached depths comparable to the pycnocline depth, z_{pyc}, these only occur at times when the pycnocline is displaced by the wave, and so do not interact significantly with the pycnocline. It is assumed that in the present experiments, mixing was not significantly enhanced. Such changes can be captured based on a blocking ratio, for example, the one used for a stationary step in Talipova et al. (2013). The ratio compares the pycnocline depth, amplitude, and depth of the float, as $B = \frac{h_1 - h_f}{a}$, where h_f is the height of the step, and is used to identify five regimes of interaction. The level of interaction with the step increased with increasing B, from the formation of K-H instability on the pycnocline, through to total reflection of the incident wave. The interactions identified here align with those for a weak interaction in Talipova et al. (2013)'s experiments, with the motion of the float here becoming an important factor in reducing the intensity of these interactions. Carr, Sutherland, et al. (2019) also identified changes to the shape of the pycnocline in experiments where the pycnocline distance from the base of the float were much less, corresponding to Moderate-Strong interactions in the Talipova et al. (2013) system of regimes, overall indicating an applicability of these regimes even to a moving obstacle, as in the case of ice.

In applying to the field, the interaction between pressure gradients induced by surface waves, and wind, would also need consideration in conjunction with the ISWs, both in terms of the motion of ice, and the flow features induced by the relative motions of the ice and fluid. A final aspect that is likely to be important in a real-ocean system is the interaction of multiple floats, where field observations indicate effects linked to the concentration, where dissipation of the IWs under ice is maximum at intermediate concentrations (Cole et al., 2018), and which should be considered in future work.

5. Conclusion

Here, the interactions between laboratory ISWs and free-floating objects representing sea ice are investigated to a simple system of a single float. Reducing the system to this single-float system interacting with a single ISW has allowed isolation of the processes and behaviors for the first time. Applying a simple model of float motion based only on the average fluid velocity in contact with the float helps to understand the behaviors that are observed in the laboratory. The development of this model makes it possible to predict the motion of a floating parcel associated with any near-surface ISW-driven velocity field, and is validated by the use of laboratory experiments. Not only is the FMM itself simple, but it can easily be applied to analytic models which take seconds to solve, rather than hours or days as required by full Navier-Stokes solving numerical models. Float velocity was dependent on both the amplitude of the wave and the length of the float, with larger waves inducing stronger motion. For larger floats, the length of interaction increases, but with a reduction in maximum velocity. Carr, Sutherland, et al. (2019) initially investigated this dependency on L_f and λ, but the exact nature of the relationship is now captured in Equation 6, which can only be identified using the larger data set enabled by this FMM and DJL solutions. The exact nature of the flow and float dynamics exists as a result of non-stationary nature of both the flow, and the float. The good fit with an energy-less model (and with DJL waves) indicates energy transfer was low, in particular for small floats, and despite an intuitive explanation for the relationship between L_f/λ and U_{max}/c based around the increasing mass/inertia of the float, such a relationship is here explained by the form of the solitary wave velocity profile alone—that is the effect on the float's velocity of the still water either side of the wave.

As sea ice in the Arctic Ocean thins and retreats, the state of the upper ocean stratification is changing, and relationships not yet fully understood are changing. This study employs a simple process experimental approach to understanding ISW-ice interactions, removing a number of real-world complexities to focus on specific relationships. Future work on ISW-ice interactions could further investigate more complex (and realistic) float geometries including roughness and increased ice depth, or multiple float systems, where collisions, and cohesion play a role. Now that fundamental dynamics have been explored, a better understanding of the energetics, specifically diapycnal mixing induced by the ice, and attenuation of the wave under ice is needed. Whilst these are difficult to achieve with the present setup, various laboratory and numerical methods are available (e.g., Zahedi et al., 2021; Zahedi et al., 2023), and would be valuable for understanding grand Arctic Ocean challenges. These include the transport and mixing of heat (Lenn et al., 2009), the fate of energy in the region (Polyakov et al., 2019) and improving understanding of how ongoing sea ice declines may impact IW energy levels in the Arctic (Guthrie et al., 2013).

Data Availability Statement

The experimental data and Float Motion Model code used in the study is be available at Newcastle University's data repository via Hartharn-Evans et al. (2023) with CC-BY 4.0 Licence.

Acknowledgments

We thank Dunphy et al. (2011) for their DJLES code used in this project, which is freely available at Dunphy (2011). Technical assistance in the Novak Laboratory at Newcastle University was provided by Jonathan Bell and Stuart Patterson and is gratefully acknowledged. This work was supported by the Natural Environment Research Council (NERC) funded ONE Planet Doctoral Training Partnership (S.H.E., Grant [NE/S007512/1]). For the purpose of open access, the author has applied a Creative Commons Attribution (CC BY) licence to any Author Accepted Manuscript version arising from this submission. Two anonymous reviewers are thanked for contributions to this manuscript.

References

Aleyasin, S. S., Tachie, M. F., & Balachandar, R. (2021). Characteristics of flow past elongated bluff bodies with underbody gaps due to varying inflow turbulence. *Physics of Fluids*, *33*(12), 125106. https://doi.org/10.1063/5.0072390

Apel, J., Holbrook, J., Liu, A., & Tsai, J. (1985). The Sulu Sea internal soliton experiment. *Journal of Physical Oceanography*, *15*(12), 1625–1651. https://doi.org/10.1175/1520-0485(1985)015⟨1625:TSSISE⟩2.0.CO;2

Bennetts, L. G., Alberello, A., Meylan, M. H., Cavaliere, C., Babanin, A. V., & Toffoli, A. (2015). An idealised experimental model of ocean surface wave transmission by an ice floe. *Ocean Modelling*, *96*, 85–92. https://doi.org/10.1016/j.ocemod.2015.03.001

Bennetts, L. G., & Williams, T. D. (2015). Water wave transmission by an array of floating discs. *Proceedings of the Royal Society A: Mathematical, Physical and Engineering Sciences*, *471*(2173), 20140698. https://doi.org/10.1098/rspa.2014.0698

Boegman, L., & Stastna, M. (2019). Sediment resuspension and transport by internal solitary waves. *Annual Review of Fluid Mechanics*, *51*(1), 129–154. https://doi.org/10.1146/annurev-fluid-122316-045049

Carr, M., Davies, P. A., & Hoebers, R. P. (2015). Experiments on the structure and stability of mode-2 internal solitary-like waves propagating on an offset pycnocline. *Physics of Fluids*, *27*(4), 046602. https://doi.org/10.1063/1.4916881

Carr, M., Stastna, M., Davies, P. A., & van de Wal, K. J. (2019). Shoaling mode-2 internal solitary-like waves. *Journal of Fluid Mechanics*, *879*, 604–632. https://doi.org/10.1017/jfm.2019.671

Carr, M., Sutherland, P., Haase, A., Evers, K. U., Fer, I., Jensen, A., et al. (2019). Laboratory experiments on internal solitary waves in ice-covered waters. *Geophysical Research Letters*, *46*(21), 12230–12238. https://doi.org/10.1029/2019GL084710

Cole, S. T., Toole, J. M., Rainville, L., & Lee, C. M. (2018). Internal waves in the Arctic: Influence of ice concentration, ice roughness, and surface layer stratification. *Journal of Geophysical Research: Oceans*, *123*(8), 5571–5586. https://doi.org/10.1029/2018JC014096

Czipott, P. V., Levine, M. D., Paulson, C. A., Menemenlis, D., Farmer, D. M., & Williams, R. G. (1991). Ice flexure forced by internal wave packets in the Arctic Ocean. *Science*, *254*(5033), 832–835. https://doi.org/10.1126/science.254.5033.832

Dalziel, S. B., Carr, M., Sveen, J. K., & Davies, P. A. (2007). Simultaneous synthetic schlieren and PIV measurements for internal solitary waves. *Measurement Science and Technology*, *18*(3), 533–547. https://doi.org/10.1088/0957-0233/18/3/001

Dorrell, R. M., Lloyd, C. J., Lincoln, B. J., Rippeth, T. P., Taylor, J. R., Caulfield, C. C. P., et al. (2022). Anthropogenic mixing in seasonally stratified shelf seas by offshore wind farm infrastructure. *Frontiers in Marine Science*, *9*, 124. https://doi.org/10.3389/fmars.2022.830927

Dunphy, M. (2011). DJLES - Dubreil-Jacotin-long equation solver [Software]. Retrieved from https://github.com/mdunphy/DJLES

Dunphy, M., Subich, C., & Stastna, M. (2011). Spectral methods for internal waves: Indistinguishable density profiles and double-humped solitary waves. *Nonlinear Processes in Geophysics*, *18*(3), 351–358. https://doi.org/10.5194/npg-18-351-2011

Ekman, V. W. (1904). On dead-water: Being a description of the so-called phenomenon often hindering the headway and navigation of ships in Norwegian Fjords and elsewhere, and an experimental investigation of its causes etc. In F. Nansen (Ed.), *The Norwegian north polar expedition 1893-1896: Scientific results* (Vol. 5, pp. 1–150). Fridtjof Nansen Fund for the Advancement of Science, Longmans, Green, and Co. Retrieved from https://digitalarchiveontario.ca/objects/276519/the-norwegian-north-polar-expedition-18931896?ctx=758b33f0d5a524c1a630610f5f8f3bdf0c7162e0&idx=5#

Fer, I., Koenig, Z., Kozlov, I. E., Ostrowski, M., Rippeth, T. P., Padman, L., et al. (2020). Tidally forced lee waves drive turbulent mixing along the Arctic Ocean margins. *Geophysical Research Letters*, *47*(16), e2020GL088083. https://doi.org/10.1029/2020GL088083

Grue, J., Jensen, A., Rusås, P. O., & Sveen, J. K. (2000). Breaking and broadening of internal solitary waves. *Journal of Fluid Mechanics*, *413*, 181–217. https://doi.org/10.1017/S0022112000008648

Guthrie, J. D., & Morison, J. H. (2021). Not just sea ice: Other factors important to near-inertial wave generation in the Arctic Ocean. *Geophysical Research Letters*, *48*(3), e2020GL090508. https://doi.org/10.1029/2020GL090508

Guthrie, J. D., Morison, J. H., & Fer, I. (2013). Revisiting internal waves and mixing in the Arctic Ocean. *Journal of Geophysical Research: Oceans*, *118*(8), 3966–3977. https://doi.org/10.1002/jgrc.20294

Hartharn-Evans, S. G., Carr, M., & Stastna, M. (2023). Interactions between internal solitary waves and sea ice [Dataset]. Newcastle University. https://doi.org/10.25405/data.ncl.c.6693927.v1

Hartharn-Evans, S. G., Carr, M., Stastna, M., & Davies, P. A. (2022). Stratification effects on shoaling internal solitary waves. *Journal of Fluid Mechanics*, *933*(A19), A19. https://doi.org/10.1017/jfm.2021.1049

Jackson, C., da Silva, J., Jeans, G., Alpers, W., & Caruso, M. (2013). Nonlinear internal waves in synthetic aperture radar imagery. *Oceanography*, *26*(2), 68–79. https://doi.org/10.5670/oceanog.2013.32

Kozlov, I. E., Zubkova, E. V., & Kudryavtsev, V. N. (2017). Internal solitary waves in the Laptev Sea: First results of spaceborne SAR observations. *IEEE Geoscience and Remote Sensing Letters*, *14*(11), 2047–2051. https://doi.org/10.1109/LGRS.2017.2749681

Kurkina, O. E., & Talipova, T. G. (2011). Huge internal waves in the vicinity of the Spitsbergen Island (Barents Sea). *Natural Hazards and Earth System Sciences*, *11*(3), 981–986. https://doi.org/10.5194/nhess-11-981-2011

Lamb, K. G. (1997). Particle transport by nonbreaking, solitary internal waves. *Journal of Geophysical Research*, *102*(C8), 18641–18660. https://doi.org/10.1029/97JC00441

Lamb, K. G., & Wan, B. (1998). Conjugate flows and flat solitary waves for a continuously stratified fluid. *Physics of Fluids*, *10*(8), 2061–2079. https://doi.org/10.1063/1.869721

Lamb, K. G., & Warn-Varnas, A. (2015). Two-dimensional numerical simulations of shoaling internal solitary waves at the ASIAEX site in the South China Sea. *Nonlinear Processes in Geophysics*, *22*(3), 289–312. https://doi.org/10.5194/npg-22-289-2015

Lenn, Y. D., Wiles, P. J., Torres-Valdes, S., Abrahamsen, E. P., Rippeth, T. P., Simpson, J. H., et al. (2009). Vertical mixing at intermediate depths in the Arctic boundary current. *Geophysical Research Letters*, *36*(5), L05601. https://doi.org/10.1029/2008GL036792

Li, J., Kohout, A. L., & Shen, H. H. (2015). Comparison of wave propagation through ice covers in calm and storm conditions. *Geophysical Research Letters*, *42*(14), 5935–5941. https://doi.org/10.1002/2015GL064715

Luzzatto-Fegiz, P., & Helfrich, K. R. (2014). Laboratory experiments and simulations for solitary internal waves with trapped cores. *Journal of Fluid Mechanics*, *757*, 354–380. https://doi.org/10.1017/jfm.2014.501

Marchenko, A. V., Morozov, E. G., Kozlov, I. E., & Frey, D. I. (2021). High-amplitude internal waves southeast of Spitsbergen. *Continental Shelf Research*, *227*, 104523. https://doi.org/10.1016/j.csr.2021.104523

Marchenko, A. V., Morozov, E. G., Muzylev, S. V., & Shestov, A. S. (2010). Interaction of short internal waves with the ice cover in an Arctic fjord. *Oceanology*, *50*(1), 18–27. https://doi.org/10.1134/S0001437010010029

Martin, T., Steele, M., & Zhang, J. (2014). Seasonality and long-term trend of Arctic Ocean surface stress in a model. *Journal of Geophysical Research: Oceans*, *119*(3), 1723–1738. https://doi.org/10.1002/2013JC009425

Morozov, E., & Pisarev, S. (2002). Internal tides at the arctic latitudes (Numerical experiments). *Oceanology*, *42*, 153–161.

Muench, R. D., LeBlond, P. H., & Hachmeister, L. E. (1983). On some possible interactions between internal waves and sea ice in the marginal ice zone. *Journal of Geophysical Research*, *88*(C5), 2819–2826. https://doi.org/10.1029/JC088iC05p02819

Munro, R. J., & Davies, P. A. (2006). The flow generated in a continuously stratified rotating fluid by the differential rotation of a plane horizontal disc. *Fluid Dynamics Research*, *38*(8), 522–538. https://doi.org/10.1016/j.fluiddyn.2006.03.002

Nansen, F. (1897). *Farthest North: Being the record of a voyage of exploration of the ship "Fram" 1893-96 and of a fifteen months' sleigh journey by Dr. Nansen and Lieut. Johansen* (Vol. 1). Constable. Retrieved from https://www.gutenberg.org/files/30197/30197-h/30197-h.htm#ch1

Osborne, A., Burch, T., & Scarlet, R. (1978). The influence of internal waves on deep-water drilling. *Journal of Petroleum Technology*, *30*(10), 1497–1504. https://doi.org/10.2118/6913-PA

Pinkel, R. (2005). Near-inertial wave propagation in the western Arctic. *Journal of Physical Oceanography*, *35*(5), 645–665. https://doi.org/10.1175/JPO2715.1

Polyakov, I. V., Padman, L., Lenn, Y. D., Pnyushkov, A., Rember, R., & Ivanov, V. V. (2019). Eastern Arctic Ocean diapycnal heat fluxes through large double-diffusive steps. *Journal of Physical Oceanography*, *49*(1), 227–246. https://doi.org/10.1175/JPO-D-18-0080.1

Polyakov, I. V., Rippeth, T. P., Fer, I., Alkire, M. B., Baumann, T. M., Carmack, E. C., et al. (2020). Weakening of cold halocline layer exposes sea ice to oceanic heat in the eastern Arctic Ocean. *Journal of Climate*, *33*(18), 8107–8123. https://doi.org/10.1175/JCLI-D-19-0976.1

Rippeth, T. P., Vlasenko, V., Stashchuk, N., Scannell, B. D., Green, J. A. M., Lincoln, B. J., & Bacon, S. (2017). Tidal conversion and mixing poleward of the critical latitude (an Arctic case study). *Geophysical Research Letters*, *44*(24), 12349–12357. https://doi.org/10.1002/2017GL075310

Saiki, R., & Mitsudera, H. (2016). A mechanism of ice-band pattern formation caused by resonant interaction between sea ice and internal waves: A theory. *Journal of Physical Oceanography*, *46*(2), 583–600. https://doi.org/10.1175/JPO-D-14-0162.1

Song, Z. J., Teng, B., Gou, Y., Lu, L., Shi, Z. M., Xiao, Y., & Qu, Y. (2011). Comparisons of internal solitary wave and surface wave actions on marine structures and their responses. *Applied Ocean Research*, *33*(2), 120–129. https://doi.org/10.1016/j.apor.2011.01.003

Squire, V. A. (2020). Ocean wave interactions with sea ice: A reappraisal. *Annual Review of Fluid Mechanics*, *52*(1), 37–60. https://doi.org/10.1146/annurev-fluid-010719-060301

Squire, V. A., & Moore, S. C. (1980). Direct measurement of the attenuation of ocean waves by pack ice. *Nature*, *283*(5745), 365–368. https://doi.org/10.1038/283365a0

Talipova, T., Terletska, K., Maderich, V., Brovchenko, I., Jung, K. T., Pelinovsky, E., & Grimshaw, R. (2013). Internal solitary wave transformation over a bottom step: Loss of energy. *Physics of Fluids*, *25*(3), 032110. https://doi.org/10.1063/1.4797455

Timco, G. W. (1980). The mechanical properties of saline-doped and carbamide (urea)-doped model ice. *Cold Regions Science and Technology*, *3*(1), 45–56. https://doi.org/10.1016/0165-232X(80)90006-3

Turner, R. E. L., & Vanden-Broeck, J.-M. (1988). Broadening of interfacial solitary waves. *The Physics of Fluids*, *31*(9), 2486–2490. https://doi.org/10.1063/1.866602

Urbancic, G. H., Lamb, K. G., Fer, I., & Padman, L. (2022). The generation of linear and nonlinear internal waves forced by subinertial tides over the Yermak Plateau, Arctic Ocean. *Journal of Physical Oceanography*, *52*(9), 2183–2203. https://doi.org/10.1175/JPO-D-21-0264.1

van der Kindere, J., & Ganapathisubramani, B. (2018). Effect of length of two-dimensional obstacles on characteristics of separation and reattachment. *Journal of Wind Engineering and Industrial Aerodynamics*, *178*, 38–48. https://doi.org/10.1016/j.jweia.2018.04.018

Vlasenko, V., Stashchuk, N., Hutter, K., & Sabinin, K. (2003). Nonlinear internal waves forced by tides near the critical latitude. *Deep Sea Research Part I: Oceanographic Research Papers*, *50*(3), 317–338. https://doi.org/10.1016/S0967-0637(03)00018-9

Wang, X., Zhou, J.-F., Wang, Z., & You, Y.-X. (2018). A numerical and experimental study of internal solitary wave loads on semi-submersible platforms. *Ocean Engineering*, *150*, 298–308. https://doi.org/10.1016/j.oceaneng.2017.12.042

Wang, Z., Pãrãu, E. I., Milewski, P. A., & Vanden-Broeck, J. M. (2014). Numerical study of interfacial solitary waves propagating under an elastic sheet. *Proceedings of the Royal Society A: Mathematical, Physical and Engineering Sciences*, *470*(2168), 20140111. https://doi.org/10.1098/rspa.2014.0111

Zahedi, S., Aghsaee, P., & Boegman, L. (2021). Internal solitary wave bottom boundary layer dissipation. *Physical Review Fluids*, *6*(7), 074802. https://doi.org/10.1103/PhysRevFluids.6.074802

Zahedi, S., Ghassemi, A., & Boegman, L. (2023). Bolus degeneration on uniform slopes. *Estuarine, Coastal and Shelf Science*, *280*, 108190. https://doi.org/10.1016/j.ecss.2022.108190

Zhang, P., Li, Q., Xu, Z., & Yin, B. (2022). Internal solitary wave generation by the tidal flows beneath ice keel in the Arctic Ocean. *Journal of Oceanology and Limnology*, *40*(3), 831–845. https://doi.org/10.1007/s00343-021-1052-7

Zhang, P., Xu, Z., Li, Q., You, J., Yin, B., Robertson, R., & Zheng, Q. (2022). Numerical Simulations of internal solitary wave evolution beneath an ice keel. *Journal of Geophysical Research: Oceans*, *127*(2), e2020JC017068. https://doi.org/10.1029/2020JC017068

Zimin, A. V., Kozlov, I. E., Atadzhanova, O. A., & Chapron, B. (2016). Monitoring short-period internal waves in the White Sea. *Izvestiya - Atmospheric and Ocean Physics*, *52*(9), 951–960. https://doi.org/10.1134/S0001433816090309